A crossed beam study of 18O(3P)+NO2 and 18O(1D)+NO2: Isotope exchange and O2+NO formation channels

Kathleen A. Mar, Annalise L. Van Wyngarden, Chi-Wei Liang, Yuan T. Lee, Jim J. Lin et al.

Citation: J. Chem. Phys. **137**, 044302 (2012); doi: 10.1063/1.4736567
View online: http://dx.doi.org/10.1063/1.4736567
View Table of Contents: http://jcp.aip.org/resource/1/JCPSA6/v137/i4
Published by the American Institute of Physics.

A crossed beam study of $^{18}O(^3P)+NO_2$ and $^{18}O(^1D)+NO_2$: Isotope exchange and O_2+NO formation channels

Kathleen A. Mar,[1,a)] Annalise L. Van Wyngarden,[2,b)] Chi-Wei Liang,[3] Yuan T. Lee,[3] Jim J. Lin,[3] and Kristie A. Boering[4,c)]
[1]*Department of Chemistry, University of California, Berkeley, California 94720, USA*
[2]*Department of Chemistry, San Jose State University, San Jose, California 95192, USA*
[3]*Institute of Atomic and Molecular Sciences, Academia Sinica, Taipei, Taiwan and Department of Chemistry, National Taiwan University, Taipei, Taiwan*
[4]*Departments of Chemistry and of Earth and Planetary Science, University of California, Berkeley, California 94720, USA*

(Received 25 November 2011; accepted 19 June 2012; published online 24 July 2012)

The products and dynamics of the reactions $^{18}O(^3P)+NO_2$ and $^{18}O(^1D)+NO_2$ have been investigated using crossed beams and provide new constraints on the structures and lifetimes of the reactive nitrogen trioxide intermediates formed in collisions of $O(^3P)$ and $O(^1D)$ with NO_2. For each reaction, two product channels are observed – isotope exchange and O_2+NO formation. From the measured product signal intensities at collision energies of ~6 to 9.5 kcal/mol, the branching ratio for O_2+NO formation vs. isotope exchange for the $O(^3P)+NO_2$ reaction is 52(+6/−2)% to 48(+2/−6)%, while that for $O(^1D)+NO_2$ is 97(+2/−12)% to 3(+12/−2)%. The branching ratio for the $O(^3P)+NO_2$ reaction derived here is similar to the ratio measured in previous kinetics studies, while this is the first study in which the products of the $O(^1D)+NO_2$ reaction have been determined experimentally. Product energy and angular distributions are derived for the $O(^3P)+NO_2$ isotope exchange and the $O(^1D)+NO_2 \rightarrow O_2+NO$ reactions. The results demonstrate that the $O(^3P)+NO_2$ isotope exchange reaction proceeds by an NO_3* complex that is long-lived with respect to its rotational period and suggest that statistical incorporation of the reactant ^{18}O into the product NO_2 (apart from zero point energy isotope effects) likely occurs. In contrast, the $^{18}O(^1D)+NO_2 \rightarrow O_2+NO$ reaction proceeds by a direct "stripping" mechanism via a short-lived ^{18}O-O-NO* complex that results in the occurrence of ^{18}O in the product O_2 but not in the product NO. Similarly, ^{18}O is detected in O_2 but not NO for the $O(^3P)+NO_2 \rightarrow O_2+NO$ reaction. Thus, even though the product energy and angular distributions for $O(^3P)+NO_2 \rightarrow O_2+NO$ derived from the experimental data are uncertain, these results for isotope labeling under single collision conditions support previous kinetics studies that concluded that this reaction proceeds by an asymmetric ^{18}O-O-NO* intermediate and not by a long-lived symmetric NO_3* complex, as earlier bulk isotope labeling experiments had concluded. Applicability of these results to atmospheric chemistry is also discussed. © *2012 American Institute of Physics*. [http://dx.doi.org/10.1063/1.4736567]

I. INTRODUCTION

The physical chemistry of the reactions between oxygen atoms and NO_2 has been studied from a number of experimental and theoretical perspectives, many of which have focused on the nature and reactivity of the nitrogen trioxide intermediates likely to be involved in the reactions. For example, the photo-excitation and decomposition of NO_3 can result in either $NO+O_2$ or $O(^3P)+NO_2$ and has served as an important model system for both experimental and theoretical investigations of the variables that control chemical reactivity in an excited molecule as it evolves to products.[1–5] For the reaction $O(^3P)+NO_2$, O_2+NO can be produced (R1), NO_3 can be produced if an excited NO_3* intermediate is stabilized by a third body (R2), or isotope exchange can occur (shown in (R3) with $^{18}O(^3P)$ as the reactant),

$$O(^3P) + NO_2 \rightarrow O_2 + NO \quad \text{(Reaction)}, \tag{R1}$$

$$O(^3P) + NO_2 + M \rightarrow NO_3^* + M \rightarrow NO_3 + M \quad \text{(3-body Association)}, \tag{R2}$$

$$^{18}O(^3P) + {}^{46}NO_2 \rightarrow {}^{16}O(^3P) + {}^{48}NO_2 \quad \text{(Isotope Exchange)}. \tag{R3}$$

Using state-specific pump-probe techniques,[6] isotope labeling,[7–10] and kinetics experiments,[11,12] it has been questioned and debated whether the intermediates formed in each of these three reactions in fact share their structures, geometries, and/or internal energy distributions with the NO_3* complex formed upon photo-excitation of NO_3, with often conflicting conclusions. In particular, it has been debated whether (R1) proceeds by a symmetric NO_3* complex

a)Present address: Air Compliance Division Environmental Protection Agency, Region 10, Seattle, Washington, USA.
b)Previously at Department of Chemistry, University of California, Berkeley, Berkeley, California 94720, USA.
c)Electronic mail: boering@berkeley.edu.

similar to that for (R2) or whether it instead proceeds by an asymmetric OONO*-type intermediate.[6–8,11,12]

There also remain unanswered questions regarding the $O(^1D)+NO_2$ reaction. The products O_2+NO may be formed (R4) or quenching of $O(^1D)$ to $O(^3P)$ can occur (R5). In addition, exchange of oxygen atoms during the collision may occur, either with (R5a) or (R6) without quenching to $O(^3P)$,

$$O(^1D) + NO_2 \rightarrow O_2 + NO \quad \text{(Reaction)}, \tag{R4}$$

$$O(^1D) + NO_2 \rightarrow O(^3P) + NO_2 \quad \text{(Quenching)}, \tag{R5}$$

$$^{18}O(^1D) + {}^{46}NO_2 \rightarrow {}^{16}O(^3P) + {}^{48}NO_2 \quad \text{(Quenching with Isotope Exchange)}, \tag{R5a}$$

$$^{18}O(^1D) + {}^{46}NO_2 \rightarrow {}^{18}O(^3P) + {}^{46}NO_2 \quad \text{(Quenching without Isotope Exchange)}, \tag{R5b}$$

$$^{18}O(^1D) + {}^{46}NO_2 \rightarrow {}^{16}O(^1D) + {}^{48}NO_2 \quad \text{(Isotope Exchange)}. \tag{R6}$$

The branching ratio for (R4):(R5) is not known since kinetics studies to date[13–16] have monitored only the loss of reactants. Furthermore, no direct information is available on the dynamics or the intermediates formed in either reaction. Analogous to (R5a) and (R6), quenching and "non-quenching" channels have been observed for the $^{18}O(^1D)+CO_2$ isotope exchange reaction, both of which were determined to proceed through a long-lived CO_3* complex.[17,18] For $O(^1D)+NO_2$, however, the extent to which isotope exchange occurs (if at all) or the characteristics and dynamics of the excited nitrogen trioxide intermediates that could facilitate isotope exchange have not been determined experimentally.

In this paper, the dynamics, reactive intermediates, and products formed upon collisions of $O(^3P)$ and $O(^1D)$ with NO_2 are explored using crossed atomic and molecular beams. This technique is particularly well-suited for distinguishing between long-lived complex formation and direct reaction mechanisms[19] and thus can directly address outstanding questions regarding the mechanisms for $O(^3P)+NO_2$ isotope exchange and O_2+NO formation, and can be used to explore for the first time the dynamics of the $O(^1D)+NO_2$ reaction. In addition, because reaction products were detected and quantified using mass spectrometry, direct identification of the reaction products and estimates of the product branching ratios for both the $O(^3P)+NO_2$ and $O(^1D)+NO_2$ reactions are obtained. Experimental and analytical details are given in Sec. II and the results and their discussion are given in Sec. III.

II. EXPERIMENT AND DATA ANALYSIS

The crossed molecular beam apparatus used in this experiment has been described previously.[18,20] Our NO_2 source was generated by bubbling ~42 psia Ne through liquid NO_2 that was kept at 20°C in a dark environment to avoid thermal or photo-dissociation of NO_2. The seeded NO_2 was expanded through an Even-Lavie pulsed valve[21] that was heated to ~212°C to ensure that the fraction of N_2O_4 in the beam was less than 5%,[22] as confirmed mass spectrometrically by measuring the NO_2^+ and $N_2O_4^+$ signals from the NO_2 beam. Furthermore, based on experiments in which we crossed an atomic beam of ^{18}O with a beam composed primarily of N_2O_4 (created by expanding room temperature NO_2 through an unheated pulsed valve), we found that N_2O_4 is less reactive towards isotope exchange than NO_2 by a factor of 4 or more and that its reactivity towards O_2+NO formation is similar to that of NO_2; we therefore conclude that possible reactive scattering of minor amounts of N_2O_4 in our NO_2 beam does not interfere with our results for $O+NO_2$.

In all experiments, the NO_2 beam was passed through a 2 mm diameter skimmer to increase its angular and velocity resolution. The NO_2 beam had an average velocity of 946 m/s, a speed ratio of 10, and an angular divergence of ±2° FWHM. Both the NO_2 beam and the ^{18}O beam (produced either by photolysis of $^{36}O_2$ or ^{18}O-labeled SO_2; see below) passed through apertures in a He-cryocooled copper plate (~20 K) that condensed effusive background gases (e.g., NO_2, O_2, and/or SO_2) from the beam sources, thus significantly improving the signal-to-noise ratio. After collision of the two reactant beams (crossed at a laboratory angle of 90°), neutral products traveled 24 cm to the detector, where they were ionized by electron impact. Product ions were selected by a quadrupole mass filter and directed to a Daly detector coupled to a multichannel scalar, which recorded product time-of-flight (TOF) spectra with 1 μs resolution; data were later rebinned to 3 or 7 μs to improve signal-to-noise. The detector was rotated about the collision point, and spectra were recorded at angles chosen to best cover the center-of-mass (COM) frame distribution of products. The laboratory-frame angular distributions were determined by integrating the signal of the background-corrected TOF spectra (see below) collected at different angles. This procedure was repeated several times to check the stability of the molecular beam intensities. Estimates of the experimental error bars for these distributions were based primarily on the signal-to-noise ratios and the magnitudes of background subtraction; possible errors from other sources (e.g., drift of the molecular beams) have also been considered and included. To extract COM product angular and kinetic energy information, background-corrected product TOF spectra in the laboratory frame were simulated using an iterative forward-convolution method,[23] in which trial COM product translational energy distributions, $P(E_T)$, and COM angular distributions, $P(\theta)$, were iteratively adjusted until satisfactory agreement with the laboratory angular and velocity distributions was achieved. The same iterative forward-convolution method was then used to evaluate the range in the $P(E_T)$s and $P(\theta)$s that could adequately simulate the data in order to estimate uncertainty in the "best-fit" $P(E_T)$ and $P(\theta)$.

In the experiments, two different methods for generating an oxygen atom beam were used. First, to obtain product TOF spectra with high energy resolution, a skimmed beam of $^{36}O_2$ was photolyzed at 157.6 nm to produce an ^{18}O beam with a very narrow speed distribution. However, the photolysis products at this wavelength are 50% $^{18}O(^3P)$ and 50% $^{18}O(^1D)$, and we found that the observed products could not

be unambiguously assigned to either $O(^3P)$ or $O(^1D)$ reactant based on these high resolution experiments alone. Second, to aid in assigning reaction products to either $^{18}O(^3P)+NO_2$ or $^{18}O(^1D)+NO_2$, photolysis of ^{18}O-labeled SO_2 at 193 nm was used as a source of pure $^{18}O(^3P)$ since production of $O(^1D)$ is energetically inaccessible for a single photon process at this wavelength. The $^{18}O(^3P)$ beam produced in this second set of experiments and the resulting product TOF spectra had significantly poorer energy resolution than using $^{36}O_2$ photolysis as a source of ^{18}O atoms, both because SO_2 photolysis produces oxygen atoms with a speed distribution[24] that is intrinsically wider than that produced by O_2 photolysis and because, in order to achieve an adequate ^{18}O signal, the SO_2 beam was not skimmed. In a third set of experiments, 157 nm photolysis of $^{36}O_2$ was again used as a source of ^{18}O but with a modified experimental setup to achieve an ^{18}O beam with a lower energy resolution and mean beam speed similar in character to the beam produced by photolysis of SO_2. The generation of these three distinct beams of atomic ^{18}O is described in detail below.

A. $^{18}O(^3P) + {}^{18}O(^1D)$ from $^{36}O_2$ photolysis

A molecular beam of $^{36}O_2$ with high energy resolution was generated using a pulsed valve (General Valve) with a backing pressure of ~64 psia, oriented nearly perpendicular to the reaction plane to reduce O_2 background in the main chamber. To produce an ^{18}O atomic beam, the $^{36}O_2$ beam was skimmed and then photolyzed at 157.6 nm by the 50–60 mJ output of a F_2 excimer laser (Lambda Physik, LPX 210i, operated at 40 or 50 Hz), which was focused to a spot size of 4 mm × 3 mm by a spherical-cylindrical MgF_2 lens. The resulting ^{18}O beam had an average velocity of 2293 m/s, a speed ratio of 28, and an angular divergence of ± 4° FWHM. When crossed with the NO_2 beam described above, the collision energy (E_c) was 9.5 ± 0.6 kcal/mol, where the reported error is based on propagation of the widths of the speed distributions of the beams.

For comparison with the SO_2 photolysis experiments, an ^{18}O atomic beam of lower speed resolution was produced by 157.6 nm photolysis of $^{36}O_2$ as described above but with two minor modifications. First, to increase the width of the speed distribution, we photolyzed an unskimmed beam of $^{36}O_2$. Second, the $^{36}O_2$ pulsed valve nozzle was rotated further (>90°) away from the main chamber to its limit as constrained by the source chamber geometry, reducing the speed of the atomic beam. The ^{18}O beam produced had an average velocity of 1885 m/s, a speed ratio of 5.3, and an angular divergence of ± 4.7° FWHM; the resulting collision energy when crossed with the NO_2 beam was 6.9 ± 2.1 kcal/mol.

B. $^{18}O(^3P)$ from photolysis of ^{18}O-labeled SO_2

An unskimmed molecular beam of SO_2 was generated by expanding ~26 psia of ^{18}O-labeled SO_2 (~96% ^{18}O, synthesized by burning sulfur powder in a Pyrex glass tube filled with $^{36}O_2$ gas) through an Even-Lavie pulsed valve, which was oriented so that the beam was angled as far from the main chamber as possible (constrained by the source chamber geometry) in order to reduce SO_2 background in the chamber. The SO_2 beam was then photolyzed by the 193 nm output of an ArF excimer laser (Lambda Physik LPX 210i, 50 Hz) focused to a spot size of 3 mm × 4 mm with two UV fused silica cylindrical lenses, producing $^{18}O(^3P)+S^{18}O(^3\Sigma^-)$. The resulting $^{18}O(^3P)$ beam had an average velocity of 1760 m/s, a speed ratio of 3, and an angular divergence of ±5.5° FWHM. When crossed with the NO_2 beam, the collision energy was 6.2 ± 3.2 kcal/mol. TOF data for these experiments were collected at a minimum of two different laser powers in order to rule out contribution from $O(^1D)$, which could be a photolysis product resulting from multiphoton absorption of SO_2.

C. Background corrections to TOF spectra

All TOF spectra for the isotope exchange product, $^{48}NO_2$, were corrected for $^{48}NO_2$ at natural abundance in the NO_2 beam that undergoes inelastic scattering with the reactant ^{18}O. This was accomplished by measuring the $^{46}NO_2$ scattering signal (from inelastic collisions of $^{46}NO_2$ with ^{18}O) at each angle, scaling it to the natural abundance of $^{48}NO_2$, and then subtracting this scaled background from the raw $^{48}NO_2$ TOF spectra. For the high resolution experiments, this correction ranged from 3% of the signal height at a laboratory angle of 20° to 20% of the signal height at 60°.

Using photolysis of SO_2 to produce the ^{18}O beam resulted in additional sources of background. TOF spectra for $^{48}NO_2$ were also corrected for inelastic scattering of $S^{16}O$ (m/e 48) in the ^{18}O beam by measuring the large $S^{18}O$ (m/e 50) scattering signal and scaling it to the abundance of ^{16}O in the ^{18}O-labeled SO_2 (~4%, determined mass spectrometrically) and then subtracting this correction from the raw $^{48}NO_2$ spectra. Similarly, the TOF spectra for $^{34}O_2$ were corrected for signal from ^{34}S ions, which result from inelastic scattering of $^{34}S^{16}O$ followed by dissociative ionization to $^{34}S^+ + {}^{16}O$. This correction was accomplished by measuring ^{32}S TOF spectra and scaling to the natural abundance of ^{34}S (~4%).

D. Data analysis

Determination of the relative contribution of $^{18}O(^3P)$ vs. $^{18}O(^1D)$ to the measured TOF spectra for the isotope exchange or the O_2+NO formation channels in the high resolution O_2 photolysis experiments was achieved by comparison of the signals measured in experiments using SO_2 photolysis vs. those for low resolution $^{36}O_2$ photolysis. The low-resolution $^{36}O_2$ photolysis data were scaled so that the $^{46}NO_2$ inelastic scattering signals were the same magnitude as those measured in the SO_2 photolysis experiments, and then this scaling factor was applied to either the $^{48}NO_2$ or the $^{34}O_2$ spectra from low-resolution $^{36}O_2$ photolysis. Although reactive scattering may also contribute some $^{46}NO_2$ signal, the reactive signal is more than an order of magnitude weaker than the inelastic scattering signal, such that scaling the experimental data from the above two O atom sources to the same intensity of $^{46}NO_2$ signals fairly accounts for the differences in beam intensities. The fact that the beam produced by $^{36}O_2$ photolysis was only 50% $^{18}O(^3P)$ was taken into account by further scaling the signal from the SO_2 photolysis

experiments by a factor of 0.5. In the case of the O_2+NO formation, the contribution of $O(^3P)$+NO_2 to the high resolution $^{34}O_2$ TOF spectra (which we found was dominated by signal from $O(^1D)$+NO_2) was estimated via the following technique. First, the $^{34}O_2$ signal from $O(^3P)$+NO_2 in the low resolution experiments with the SO_2 photolysis source[25] was fit using the iterative forward-convolution method. Next, the angular and translational energy distributions from the fit to the $O(^3P)$+NO_2 data were used to simulate the $^{34}O_2$ signal from $O(^3P)$+NO_2 under the conditions of the high resolution experiments. The relative magnitude of the contribution of the $O(^3P)$ reactant to the high resolution $^{34}O_2$ signal was estimated based on a comparison of the magnitudes of the low resolution data using the SO_2 and O_2 photolysis sources, assuming that the relative contributions of $O(^3P)$ vs. $O(^1D)$ are about the same for both the high- and low-resolution O_2 photolysis sources. Based on this analysis, the simulated $O(^3P)$+NO_2 signal was scaled so that its peak height was 1/6 of the high resolution signal at 40° and then removed from the high resolution $^{34}O_2$ TOF spectra. Finally, the remaining TOF signals, which at this point represented the contribution of the $O(^1D)$ reactant, were then fit with the appropriate $P(E_T)$ and $P(\theta)$ using the iterative forward convolution method. In order to evaluate the robustness of this analysis, this procedure was iteratively repeated, varying both the $P(E_T)$ and $P(\theta)$ used to simulate the laboratory velocity and angular data for $O(^3P)$+NO_2 (within a range that still resulted in reasonable fit to the data[3]) and the factor used to scale the simulated correction for $O(^3P)$+NO_2 (which was varied between 1/4 and 1/8). This analysis allowed for an evaluation of the level of uncertainty associated with using the high resolution $^{34}O_2$ data with a correction for signal from $O(^3P)$+NO_2 to draw conclusions about the COM angular and energy distributions that characterize the $O(^1D)$+NO_2 reaction.

Product branching ratios for $^{18}O(^3P)$+NO_2 and $^{18}O(^1D)$+NO_2 were calculated based on the relative signal intensities for O_2+NO formation vs. isotope exchange (i.e., (R1) vs. (R3) and (R4) vs. (R5a), respectively). For these calculations, the Jacobian factor for transforming the signal intensity from the laboratory to the COM frame and the product cross sections[26] and fragmentation ratios[27] for electron impact ionization at 70 eV were also taken into account. The transmission efficiency of the quadrupole mass filter was assumed to be the same for masses 32, 34, 46, and 48. Details of how uncertainties in the branching ratios were estimated are included in the discussion of results below.

III. RESULTS AND DISCUSSION

The crossed beam results are presented and discussed below, first for the isotope exchange channels for the $O(^3P)$+NO_2 and $O(^1D)$+NO_2 reactions ((R3) and (R5a)) for which the $^{48}NO_2$ product was measured (Sec. III A), then for the reactive channels for these reactions that produce O_2 and NO ((R1) and (R4)) for which $^{34}O_2$ was the primary product measured, among other products (Sec. III B). In Sec. III C, the branching ratios for isotope exchange versus O_2+NO for the two reactions are estimated and discussed, followed by a brief discussion of atmospheric implications in Sec. III D.

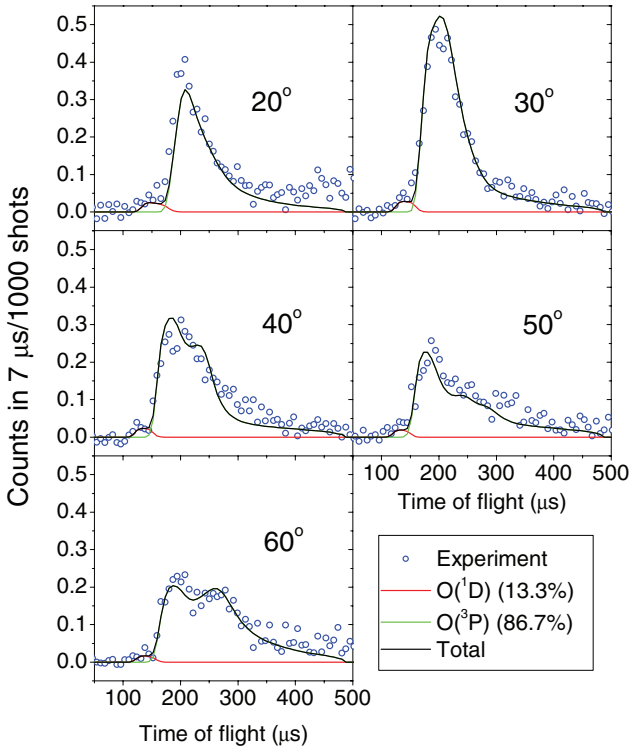

FIG. 1. High resolution time-of-flight spectra for $^{48}NO_2$ (corresponding to isotope exchange products) at 5 different laboratory angles. Experimental data are plotted as open circles; solid lines are the simulated results using the best-fit COM $P(\theta)$ and $P(E_T)$ distributions shown in Figure 4.

A. Isotope exchange channels for $O(^3P)$+NO_2 and $O(^1D)$+NO_2

High-resolution, background-corrected TOF spectra for the $^{48}NO_2$ product (symbols) and simulated spectra (lines) are shown in Figure 1 for five laboratory angles, illustrated in

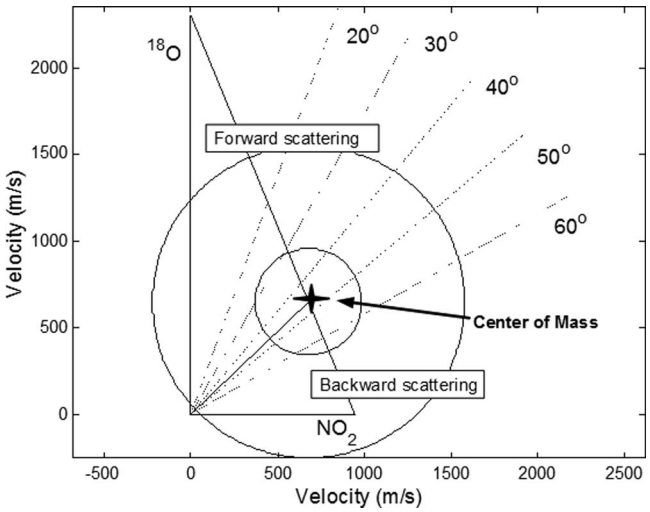

FIG. 2. Newton diagram for isotope exchange products in the high resolution ^{18}O+NO_2 crossed beam experiment. The 0° laboratory angle is defined as the direction of the ^{18}O velocity vector; the laboratory angle of the center of mass is ~46°. The inner circle corresponds to the $^{48}NO_2$ peak at ~200 μs, assigned to $O(^3P)$+NO_2 isotope exchange (R3). The outer circle corresponds to the average velocity of the fast shoulder, assigned to $O(^1D)$+NO_2 quenching with isotope exchange (R5a). Dotted lines represent laboratory angles at which scattering was sampled.

the Newton diagram of Figure 2. The main feature is a broad peak, centered around a TOF of approximately 200 μs. In addition, a small, fast shoulder is evident at all laboratory angles and is most obvious at 40° and 50°. The translational energy distribution corresponding to the major peak at 200 μs exhibits a maximum energy release equal to the collision energy. Thus, the major peak could in principle be from $O(^3P)$ isotope exchange (R3) and/or $O(^1D)$ isotope exchange without quenching (R6) since the ^{18}O beam in this experiment is 50% $^{18}O(^3P)$ and 50% $^{18}O(^1D)$ and R3 and R6 are both isothermal. In contrast, the fast shoulder corresponds to a maximum translational energy release that is significantly greater than the collision energy of 9.5 kcal/mol and therefore must result from (R5a), $O(^1D)$ isotope exchange with electronic quenching to $O(^3P)$, which is exothermic by ~46 kcal/mol.

The ambiguity in the origin of the major isotope exchange peak can be resolved using the low-resolution $^{48}NO_2$ TOF spectra shown in Figure 3, which show that the $^{48}NO_2$ peak shape and peak position for both the SO_2 photolysis experiments (producing only $^{18}O(^3P)$) and the $^{36}O_2$ photolysis experiments (producing both $^{18}O(^1D)$ and $^{18}O(^3P)$) are identical to within experimental uncertainties. Based on a detailed comparison of the magnitudes of the $^{48}NO_2$ signal from the high and low resolution experiments (see Sec. II), we therefore conclude that 97 ± 12% of the major isotope exchange peak using $^{36}O_2$ photolysis as a source of ^{18}O is from $^{18}O(^3P)+NO_2$ isotope exchange (R3), where the reported uncertainty is $\pm 1\sigma$ based on comparison of the scaled signal intensities at three different laboratory angles. Further evidence that the $^{18}O(^3P)+NO_2$ isotope exchange channel is responsible for close to 100% of the major TOF peak in Figure 1 is the fact that the $^{48}NO_2$ TOF spectra from the SO_2 photolysis experiments can be simulated (see Figure S1 in the supplementary material[25]) with a $P(\theta)$ and $P(E_T)$ that are very similar in shape (see Figure S2 in the supplementary material[25]) to the $P(\theta)$ and $P(E_T)$ for the $^{18}O(^3P)+NO_2$ isotope exchange channel (see Figure 4) that are the best fit to the high-resolution laboratory angular (Figure 5) and velocity (Figure 1) distributions for this reaction, although a very minor contribution to the results in Figure 1 from $O(^1D)+NO_2$ isotope exchange without quenching (R6) cannot be ruled out. These results are summarized in Table I.

Given the COM product $P(\theta)$ and $P(E_T)$ distributions in Figure 4 that best simulate the laboratory velocity and angular distributions for the $^{48}NO_2$ isotope exchange reaction (shown in Figures 1 and 5, respectively), it is evident that the dominant $O(^3P)+NO_2$ isotope exchange signal (the major peak in Figure 1) is best fit with an angular distribution

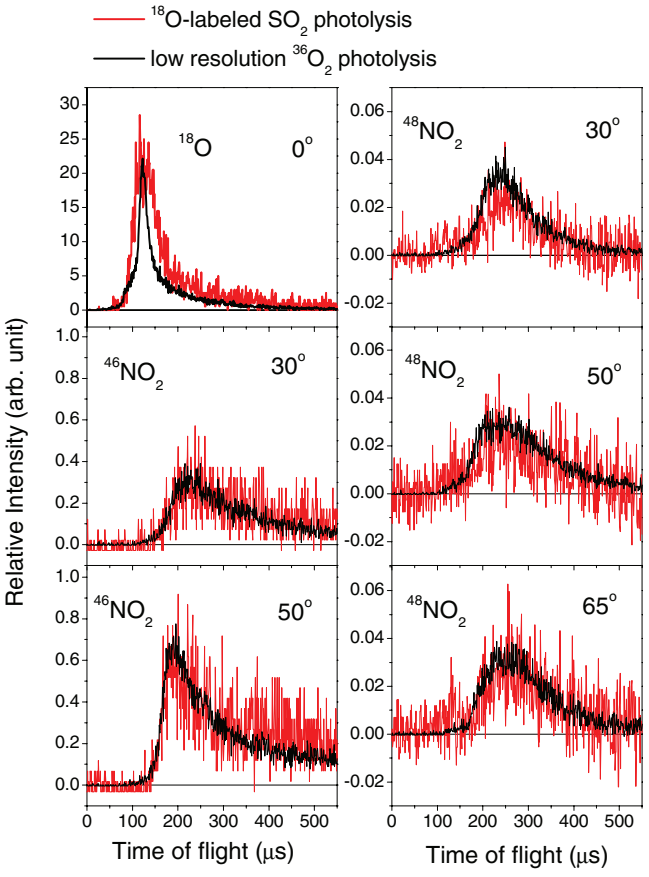

FIG. 3. Left panel: Comparison of the ^{18}O beam profile and $^{46}NO_2$ scattering signal (mostly from inelastic scattering that is much more intense than reactive scattering) for experiments using ^{18}O-labeled SO_2 photolysis (red) and low resolution $^{36}O_2$ photolysis (black) as a source of ^{18}O. Right panel: Comparison of the $^{48}NO_2$ isotope exchange signals from the two experiments; the small $^{48}NO_2$ peak observable at TOFs < 150 μs for the SO_2 photolysis source is a result of multiphoton absorption of SO_2 (see Sec. II), and is ignored in the analysis since it is well separated in time from the main peak. Angles indicated are in the laboratory frame. Signals from the experiments using the $^{36}O_2$ photolysis source (^{18}O, $^{46}NO_2$, and $^{48}NO_2$) have been universally scaled by a factor of 0.05 (see text). In the right panel, $^{48}NO_2$ signal from the experiments using the SO_2 photolysis source have been scaled by a factor of 0.5. Note the different y-axis scales.

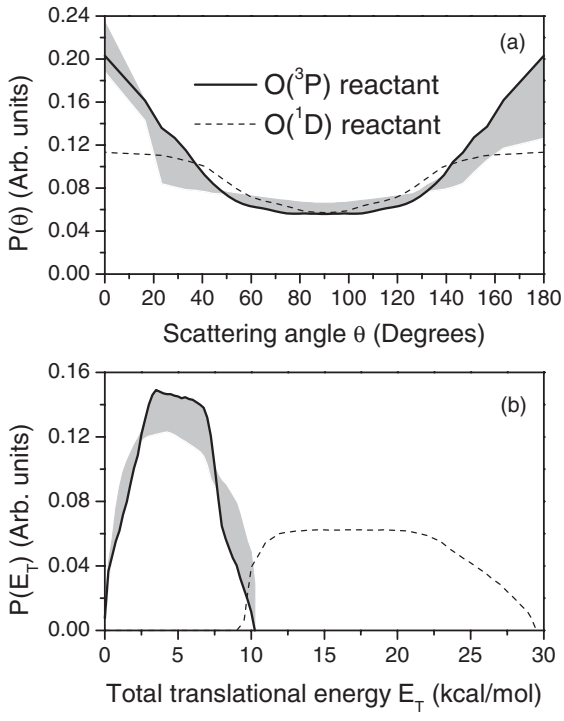

FIG. 4. (a) COM product angular distributions $P(\theta)$, and (b) COM product translational energy distributions $P(E_T)$ used to simulate the high resolution $^{48}NO_2$ TOF data, which is the product of the isotope exchange channels (R3) and (R5a). Solid curves represent the $O(^3P)+NO_2$ reaction (R3) and dashed curves represent the $O(^1D)+NO_2$ reaction (R5a). Gray shading indicates the range of $P(\theta)$s and $P(E_T)$s that adequately simulated the $O(^3P)+NO_2$ data (not shown for the $O(^1D)+NO_2$ data; see text).

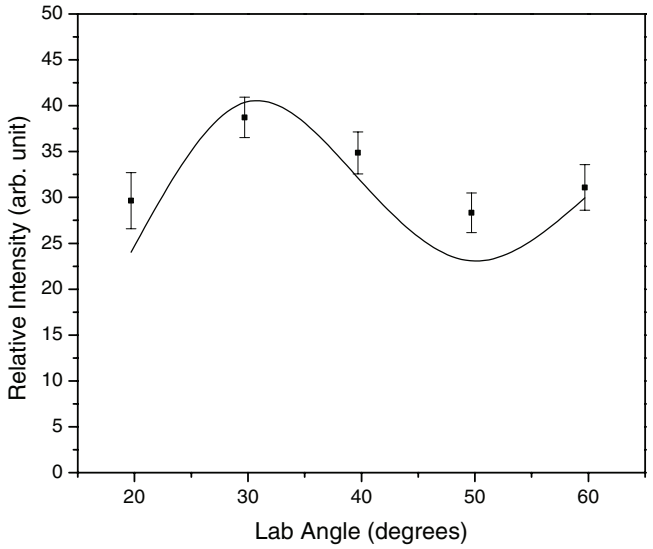

FIG. 5. Laboratory angular distribution of the $^{48}NO_2$ product from the reaction $^{18}O(^3P)+NO_2$ (R3). Filled squares are the experimental data shown with $\pm 2\sigma$ error bars; the solid line is the simulation of the laboratory data using the best-fit COM $P(\theta)$ and $P(E_T)$ distributions shown in Figure 4.

that is forward-backward symmetric, indicating that the reaction proceeds via an NO_3* intermediate that is long lived with respect to its rotational period (although a small contribution from a fraction of collisions proceeding via a direct isotope exchange mechanism resulting in a slight forward bias that is within experimental uncertainty cannot be completely ruled out). These results thus provide the first direct dynamical evidence for the long-lived complex mechanism proposed by Klein and Herron[28,29] based on bulk kinetics studies of $O(^3P)+NO_2$ isotope exchange. Furthermore, based on spectroscopic studies that indicate a high density of NO_3 vibrational states, Mikhaylichenko *et al.*[3] suggested that intramolecular vibrational redistribution (IVR) in NO_3* complexes is an efficient process. Together, these results suggest that, in the $^{18}O(^3P)+NO_2$ isotope exchange reaction, the reactant ^{18}O is likely incorporated into the product NO_2 with close to statistical probability (apart from zero-point energy isotope effects).

From the COM translational energy distribution for the $O(^3P)+NO_2$ isotope exchange products (Figure 4) that best fits the laboratory data, we find that the average translational energy release, $\langle E_T \rangle$, for $O(^3P)+NO_2$ isotope exchange is 4.8 kcal/mol, corresponding to ~50% of the available energy (i.e., the collision energy), as summarized in Table II. The remaining 50% of the available energy is partitioned into vibrational and rotational energy of the $^{48}NO_2$ product.

Similar to the analysis for $O(^3P)+NO_2$ isotope exchange above, products from $O(^1D)+NO_2$ isotope exchange with quenching (R5a) – the small, fast shoulder in the TOF spectra in Figure 1 – can also be fit with a forward-backward symmetric angular distribution (dashed lines in Figure 4). The uncertainty (not plotted) in the $P(\theta)$ for $O(^1D)+NO_2$ isotope exchange with quenching is much larger than that for $O(^3P)+NO_2$ isotope exchange, however, both because of its poor signal-to-noise ratio and because its backward scattering region was not sampled (Figure 2). Nevertheless, this experiment positively identifies isotope exchange with quenching (R5a) as one product channel of $^{18}O(^1D)+NO_2$ for the first time. Quenching without isotope exchange (R5b) also likely occurs but was not detectable under our experimental conditions. These results are summarized in Table I.

Finally, we note that, in the best fit to the high resolution $^{48}NO_2$ isotope exchange data (Figure 1), the fast shoulder assigned to $O(^1D)+NO_2$ isotope exchange with quenching (R5a) comprises 13% of the total signal intensity in the center-of-mass frame, while the major peak assigned to $O(^3P)+NO_2$ isotope exchange (R3) comprises the remaining 87%. These

TABLE I. Summary of experimental results for the $^{18}O(^3P)+NO_2$ and $^{18}O(^1D)+NO_2$ reactions.

	Product channel		Isotope-specific products	Detected?	$P(\theta)$	Inferred NO_3* inter-mediate	Branching ratio
$^{18}O(^3P) + {}^{46}NO_2 \rightarrow$							
(R1)	O_2+NO formation	(R1a)	$^{34}O_2+{}^{30}NO$	Yes		O-O-NO*	52 (+6/−2)%
		(R1b)	$^{32}O_2+{}^{32}NO$	No[a]			-
(R3)	Isotope exchange		$^{16}O(^3P)+{}^{48}NO_2$	Yes	Forward-backward symmetric	NO_3*	48 (+2/−6)%
$^{18}O(^1D) + {}^{46}NO_2 \rightarrow$							
(R4)	O_2+NO formation	(R4a)	$^{34}O_2+{}^{30}NO$	Yes	Forward peaking	O-O-NO*	97 (+2/−12)%
		(R4b)	$^{32}O_2+{}^{32}NO$	No			-
(R5)	Quenching with isotope exchange	(R5a)	$^{16}O(^3P)+{}^{48}NO_2$	Yes	Forward-backward symmetric[b]	NO_3*	3 (+12/−2)%
	Quenching without isotope exchange	(R5b)	$^{18}O(^3P)+{}^{46}NO_2$	No[c]			-
(R6)	Isotope exchange without quenching		$^{16}O(^1D)+{}^{48}NO_2$	No[d]			-

[a]Taking into account the level of background at m/e 32 in the high resolution experiments at TOFs between 60 and 140 μs in Figure 11, we estimate that the $^{32}O_2+{}^{32}NO$ products from (R1b) must be at least 4 times less abundant than the $^{34}O_2+{}^{30}NO$ products from (R1a) (the magenta curve in Figure 11), and thus below detection in this experiment.
[b]But with significant uncertainty (see text).
[c]Since the (R5a) channel is detected and quantified (and appears to proceed via a long-lived NO_3* complex), then the (R5b) reaction also likely occurs. Such a channel did not appear in $^{46}NO_2$ TOF spectra (not shown), but if the magnitude were similar to that for (R5a) or smaller (e.g., ~50% that for (R5a), as might be expected from statistical isotope exchange, apart from small zero-point energy effects), then the (R5b) signal would not have been detectable above the large background from the NO_2 source.
[d]This reaction may occur but was not detectable. For example, if the (R6) intensity were approximately the same as for (R5a), then it would be masked in the Figure 1 data by the much larger $^{48}NO_2$ signal from (R3).

TABLE II. Product energy distributions[a] and P(θ) characteristics for the $O(^3P)+NO_2$ isotope exchange and $O(^1D)+NO_2 \rightarrow O_2+NO$ reactions.

	Reaction	$\langle E_T \rangle$ (kcal/mol)	$\langle E_{int} \rangle$ (kcal/mol)	f_{int}[b]	P(θ)
(R3)	$O(^3P)+NO_2$ isotope exchange	4.8	4.7	0.50	Forward-backward symmetric
(R4a)	$O(^1D)+NO_2 \rightarrow O_2+NO$	40.7	60.8	0.60	Forward peaking

[a]For experiments with $E_{coll} = 9.5 \pm 0.6$ kcal/mol.
[b]$f_{int} = \langle E_{int} \rangle / (\langle E_{int} \rangle + \langle E_T \rangle)$.

results suggest that $O(^3P)$ is approximately 6-7 times more likely to exchange oxygen atoms with NO_2 than $O(^1D)$ at a collision energy of 9.5 kcal/mol.

B. O_2+NO formation channels for $O(^1D)+NO_2$ and $O(^3P)+NO_2$

For the O_2+NO formation channels [(R1) and (R4)], a comparison of the low resolution $^{34}O_2$ product spectra from the SO_2 and O_2 photolysis experiments (Figure 6, red and black lines, respectively) demonstrates that the signal from $^{18}O(^3P)+NO_2$ (R1) is small compared to the signal from $^{18}O(^1D)+NO_2$ (R4). As explained in Sec. II, we can therefore isolate the $^{34}O_2$ product signal from the $^{18}O(^1D) + {}^{46}NO_2 \rightarrow {}^{34}O_2 + {}^{30}NO$ reaction ((R4a) in Table I) in the high resolution experiment by subtracting the small contribution from the $^{18}O(^3P) + {}^{46}NO_2 \rightarrow {}^{34}O_2 + {}^{30}NO$ reaction ((R1a) in Table I); the resulting TOF spectra for (R4a) are shown in Figure 7, while the laboratory angular distribution is shown in Figure 8. We note that the measured peak, centered around a TOF of ~90 μs, is well separated from background measured at long TOFs at 20° that arises from the effusion of $^{34}O_2$ from the source chamber at 0° (Figure 7). Similarly, the $^{34}O_2$ peak is well-separated from the background at long TOFs measured at 75° and 105°, which we attribute to products of beam-surface reactions. While this background is no longer well-separated from the signal at 120°, the TOF spectra at 120° provide a valuable upper bound for the magnitude of the signal at 180° in the COM frame, as evident in the Newton diagram in Figure 9.

Before proceeding to discussion of the $^{34}O_2$ TOF spectra results in Figure 7 for the $^{18}O(^1D)+NO_2$ reaction (R4a), we note that scattering data for ^{30}NO – the complementary product in (R4a) – were also collected (not shown). Although the TOF spectra for ^{30}NO are noisier than those for $^{34}O_2$ due to the large ^{30}NO background from dissociative ionization of $^{46}NO_2$ in the mass spectrometer, we found that the ^{30}NO products are momentum-matched to the $^{34}O_2$ products, indicating that both $^{34}O_2$ and ^{30}NO are formed via the same reaction channels. For the O_2 photolysis experiments, the predominant reaction responsible for the ^{30}NO signal is $^{18}O(^1D)+NO_2$ (R4a), with a small contribution from $^{18}O(^3P)+NO_2$ ((R1a) in Table I).

The COM product angular and energy distributions used to simulate the $^{34}O_2$ data from $^{18}O(^1D)+NO_2$ (i.e., for (R4a)) in Figure 7 and Figure 8 are shown in Figure 10; shaded regions indicate the range of P(θ)s and P(E_T)s that adequately simulate the data, including uncertainties based on uncertainties in the size and angular distribution of the simulated contribution of $O(^3P)+NO_2$ to the total high resolution $^{34}O_2$ signal. The COM angular distribution for $^{34}O_2$ formation from (R4a) is strongly forward peaking, indicating that $^{18}O(^1D)+NO_2$ proceeds by a direct reaction mechanism.[19] This direct "stripping" mechanism is furthermore consistent with a short-lived ^{18}O-O-NO* intermediate in which the NO moiety acts as a virtual spectator, as opposed to an NO_3* intermediate similar to that inferred in this work for $O(^3P)+NO_2$ isotope exchange in which all three oxygen atoms are (at least transiently) bonded to the nitrogen atom.

Further evidence that (R4) proceeds by a direct mechanism via an ^{18}O-O-NO* intermediate rather than a symmet-

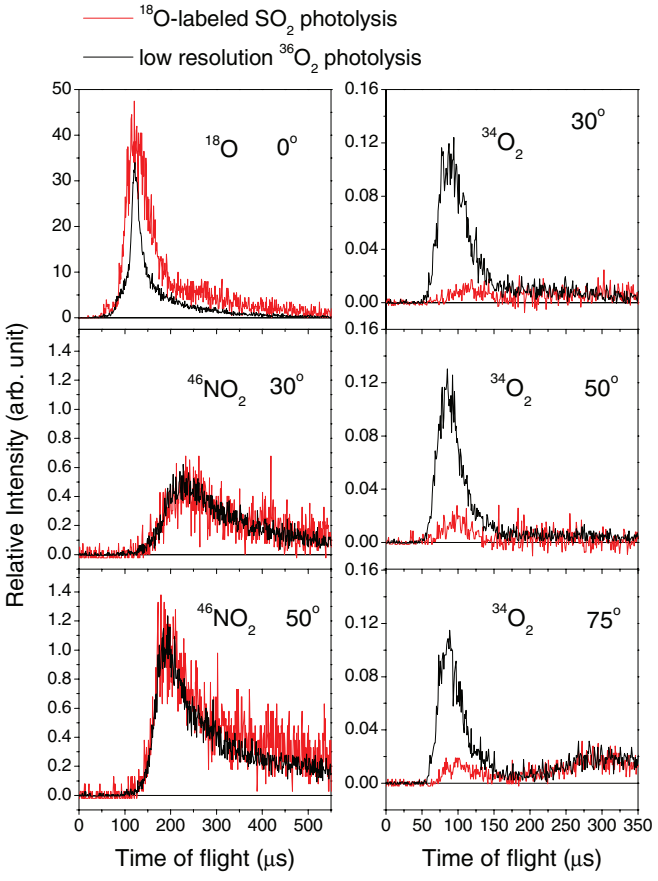

FIG. 6. Left panel: Comparison of the ^{18}O beam profile and $^{46}NO_2$ scattering signal for experiments using SO_2 photolysis (red) and low resolution $^{36}O_2$ photolysis (black) as a source of ^{18}O. Right panel: Comparison of $^{34}O_2$ signals from the two experiments. All angles indicated are in the laboratory frame, and signals (^{18}O, $^{46}NO_2$, and $^{48}NO_2$) from the experiments using the $^{36}O_2$ photolysis source have been scaled by a factor of 0.08. In the right panel, $^{34}O_2$ signal from the experiments using the SO_2 photolysis source have been scaled by a factor of 0.5. Note the different x- and y-axis scales.

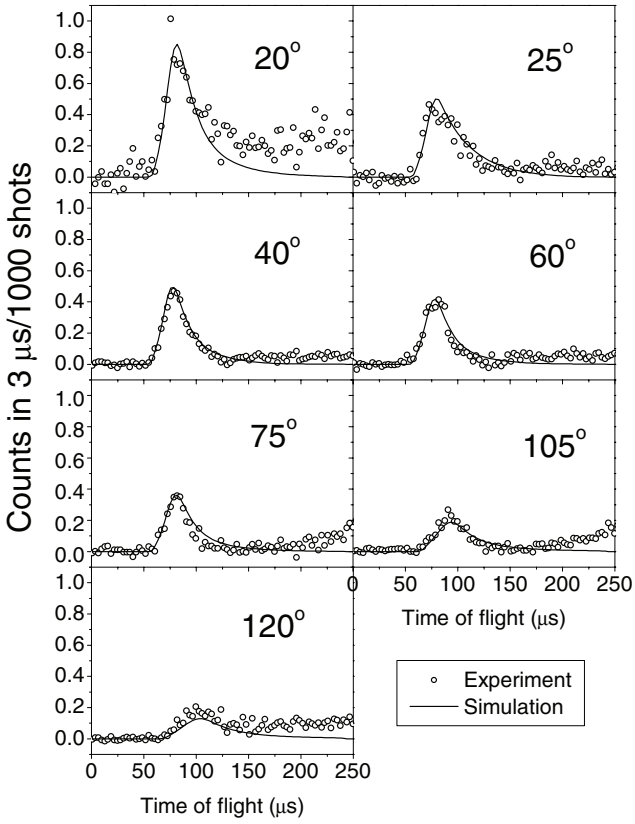

FIG. 7. High resolution time-of-flight spectra for $^{34}O_2$ from $^{18}O(^1D)+NO_2$ (R4a) at 7 different laboratory angles (open circles). Solid lines are a simulation of the data using the $P(\theta)$ and $P(E_T)$ distributions shown in Figure 10. The small contribution of $^{34}O_2$ from $^{18}O(^3P)+NO_2$ (R1a) has been subtracted (see text).

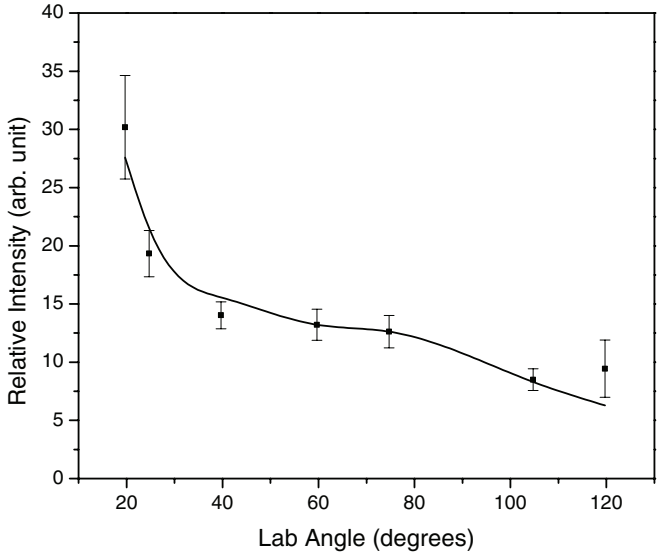

FIG. 8. Laboratory angular distribution of the $^{34}O_2$ product from the reaction $^{18}O(^1D)+NO_2$. Filled squares are experimental data shown with $\pm 2\sigma$ error bars; the solid line is the simulation of the laboratory data using the best-fit COM $P(\theta)$ and $P(E_T)$ distributions shown in Figure 10.

ric NO_3* intermediate is the fact that the reactant ^{18}O is detected in the product O_2 but not in the product NO. For example, TOF spectra for m/e 32 shown in Figure 11 (green circles) show no fast peaks analogous to those detected for $^{34}O_2$ and ^{30}NO that would correspond to the $^{32}O_2 + {}^{32}NO$ products from (R4b) in Table I. (Note that the broad, slow peak in m/e 32 centered around a TOF of 200 μs at 40° in the laboratory frame is not a result of $^{32}O_2 + {}^{32}NO$ produced by $^{18}O(^1D) + NO_2$ (R4b); rather, the magnitude, shape and timing of this peak all suggest that it results from dissociative ionization in the mass spectrometer of the $^{48}NO_2$ product from (R3) (i.e., $^{48}NO_2 + e^- \rightarrow {}^{32}NO^+ + {}^{16}O + e^-$) since NO^+ is the dominant fragment from electron impact ionization of NO_2. In summary, the forward-peaking $P(\theta)$ and the absence of reactant ^{18}O in the NO product both point to a stripping mechanism and a short-lived O-O-NO* intermediate for the $^{18}O(^1D)+NO_2 \rightarrow O_2+NO$ reaction, as summarized in Table I.

The translational and internal energy distributions of the $^{34}O_2$ products provide additional insights into the reaction dynamics and mechanism for $^{18}O(^1D)+NO_2 \rightarrow O_2+NO$ (R4). The available energy is ~102 kcal/mol (the sum of the collision energy and the reaction exothermicity), while we calculate that the average translational energy release for (R4) is 40.7 kcal/mol, or 40% of the available energy (Table II). Thus, on an average 60% of the available energy (60.8 kcal/mol) is partitioned into the internal energy of the NO and O_2 products. This large amount of product internal energy, and the fact that both $O_2(a^1\Delta_g)$ and $O_2(b^1\Sigma_g^+)$ are energetically accessible (lying 22.6 and 37.7 kcal/mol above the $O_2(X^3\Sigma_g^-)$ ground state, respectively), suggest the participation of one or more excited electronic states of O_2. (Excited electronic states of NO are inaccessible at the experimental collision energies.) On the other hand, if O_2 is formed in its ground electronic state, extremely high vibrational excitation would be required for one or both of the O_2 and NO products. Even though the TOF spectra do not allow us to distinguish between rotational, vibrational, and electronic excitation of the reaction products, significant vibrational excitation in the O_2 product with correspondingly little NO vibrational excitation might be expected in either case, based simply on the direct stripping

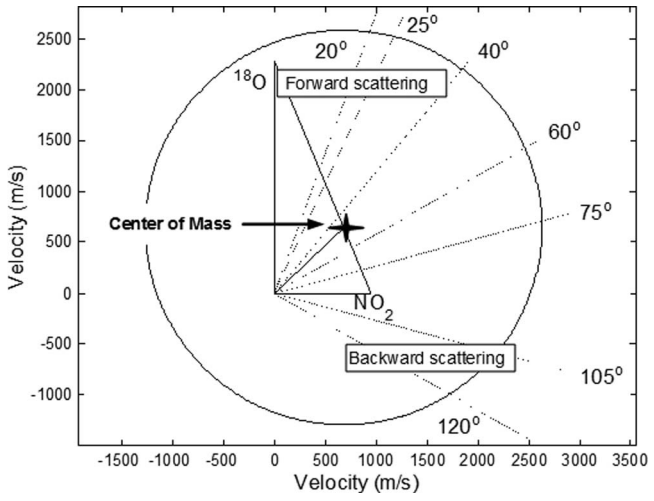

FIG. 9. Newton diagram showing the $^{34}O_2$ products for the high resolution $^{18}O+NO_2$ crossed beam experiment. The circle represents the COM velocity that corresponds to the 90 μs peak observed in the 20° TOF data. Dotted lines represent laboratory angles at which scattering was sampled.

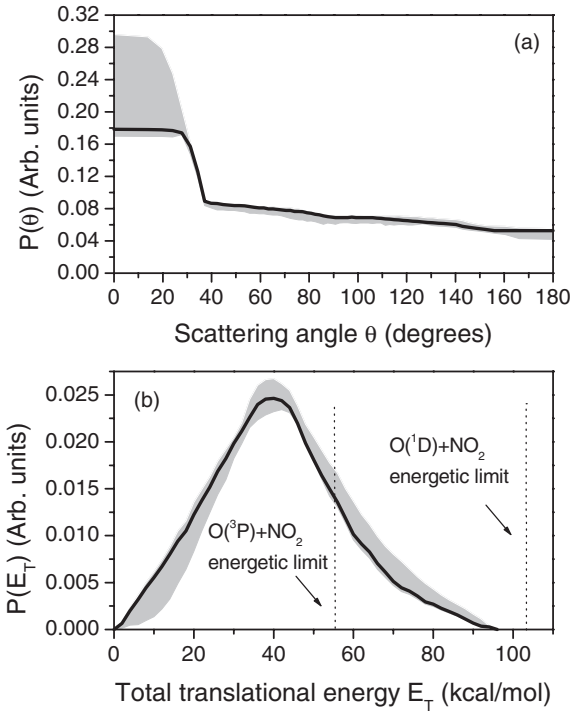

FIG. 10. Solid lines show the COM (a) P(θ) and (b) P(E_T) distributions that best simulate the $^{34}O_2$ TOF signal from $O(^1D)+NO_2$ (R4a) in Figure 7. Gray shading indicates the range of uncertainty in P(θ) and P(E_T).

mechanism inferred for (R4), in which the transfer of the O atom from NO_2 to the newly formed O_2 molecule occurs rapidly and without significant force transferred from the "attacking" O atom to the "spectator" NO moiety.

We can also gain insight into the mechanism for the $O(^3P)+NO_2 \rightarrow O_2+NO$ reaction (R1), albeit with larger uncertainties than for the $O(^1D)+NO_2 \rightarrow O_2+NO$ reaction (R4) discussed above. Although the signal for (R1) in the high resolution $^{34}O_2$ scattering experiments is too small to extract P(θ) and P(E_T) distributions, the distributions can be extracted from the low resolution SO_2 photolysis experiments (shown in Figure S3 in the supplementary material[25]). The best-fit P(θ) is not forward-backward symmetric (shown in Figure S4[25]) and is therefore suggestive of a direct stripping mechanism (although the uncertainties are quite large primarily due to interference from ^{34}S). Consistent with this picture are the detection of the ^{18}O reactant in the product O_2 but not in the product NO for the $O(^3P)+NO_2$ reaction (R1). Specifically, while $^{34}O_2$ products from $O(^3P)+NO_2$ were observed in both the high and low resolution experiments, TOF spectra for m/e 32 (Figure 11) show no peaks analogous to those observed for $^{34}O_2$ that might correspond to $^{32}O_2+^{32}NO$ products from (R1) (i.e., (R1b) in Table I). The fact that products from (R1a) but not from (R1b) were detected under single collision conditions is also consistent with $^{18}O(^3P)+NO_2 \rightarrow O_2+NO$ proceeding via an ^{18}O-O-NO* peroxo nitrate-type intermediate, in which the reactant ^{18}O ends up exclusively in the O_2 rather than the NO product. These results are summarized in Table I.

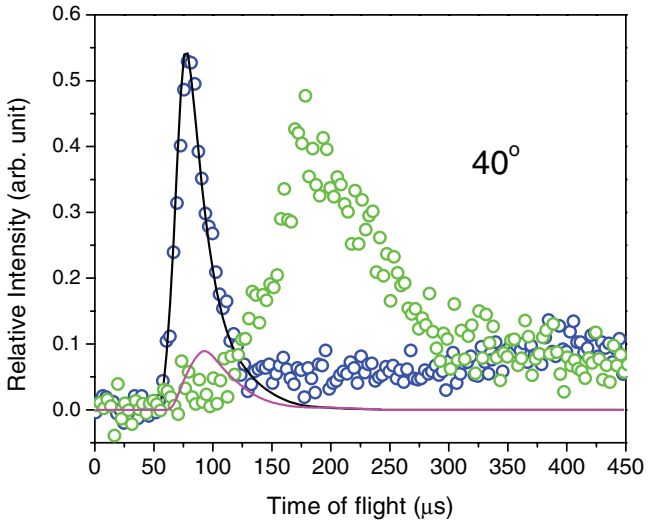

FIG. 11. Comparison of the high-resolution TOF spectrum for m/e 32 (green circles) with the high resolution TOF spectrum for $^{34}O_2$ (blue circles) at a laboratory angle of 40°. The black line is a simulation of the total $^{34}O_2$ data (from (R1a) and (R4a)) and the magenta line is a simulation of the contribution of $O(^3P)+NO_2$ (R1a) to the $^{34}O_2$ signal. The broad, slow peak centered around 200 μs in the m/e 32 TOF spectrum (green circles) is a result of dissociative ionization of $^{48}NO_2$ from (R3) to form $^{32}NO^+$ in the mass spectrometer and not production of either $^{32}O_2$ or ^{32}NO from (R4b) (see text).

These new results strengthen arguments made by previous investigators that (R1) proceeds by a direct mechanism rather than a long-lived symmetric NO_3* complex.[6,11,12] In particular, Troe[11,12] analyzed kinetics data and showed that the rate coefficient for O_2+NO formation from $O(^3P)+NO_2$ (R1) does not depend on pressure near the high-pressure limit for NO_3 formation (R2) and concluded that (R1) and (R2) are noncompeting channels of $O(^3P)+NO_2$ that proceed by different intermediates – conclusions which are consistent with the results presented here. Our results are also consistent with the conclusions of Smith *et al.*,[6] who argued for a direct stripping mechanism for (R1) based on measurements of the vibrational state distribution in the O_2 and NO products, in which they found that O_2 was formed highly vibrationally excited but that NO was formed primarily in $\upsilon = 0$. We also note that the fact that we detected ^{18}O in the O_2 but not the NO product of (R1) under single collision conditions undermines the analysis of Clyne and Thrush;[7,8] they studied isotopically labeled $^{18}O(^3P)+NO_2 \rightarrow O_2+NO$ under bulk conditions and observed a statistical distribution of ^{18}O in the reaction products, from which they concluded that (R1) proceeds via a symmetric NO_3* intermediate in which all three oxygen atoms are equivalent. Our crossed beam results suggest that, instead, the statistical distribution of ^{18}O in the reaction products they measured was controlled by $^{18}O+NO_2$ (or $^{18}O+NO$) isotope exchange reactions occurring under the multiple collision conditions of their experiment and not a symmetric NO_3* intermediate for (R1), as was first suggested by Benson.[9] Finally, we note that, overall, our results are entirely consistent with photodissociation studies of NO_3.[1,5] In Davis *et al.*,[1] as in the recent ion imaging experiment by Grubb *et al.*,[5] the symmetric NO_3 molecule is shown to dissociate exclusively to the $O+NO_2$ channel and not to the O_2+NO channel once NO_3 is excited above the threshold for the $O+NO_2$ channel. This is consistent with our combined crossed beam results showing that O_2+NO products

arise from a (short-lived) peroxy intermediate rather than a symmetric NO_3 complex.

C. Estimated product channel branching ratios for $O(^3P)+NO_2$ and $O(^1D)+NO_2$

Branching ratios for O_2+NO formation versus isotope exchange for the reactions $^{18}O(^3P)+NO_2$ and $^{18}O(^1D)+NO_2$ were estimated from the relative product signal intensities in the results presented above. For $^{18}O(^3P)+NO_2$, the $^{34}O_2$ and $^{48}NO_2$ signal intensities from the low resolution experiments yield a branching ratio for O_2+NO formation versus isotope exchange (i.e., (R1) to (R3)) of 52(+6/−2)% to 48(+2/−6)% at the experimental collision energy of 6.2 ± 3.2 kcal/mol, where the primary values given represent the best-fits to the data and the uncertainty ranges reflect the ranges of fit parameters that are still consistent with the experimental results. For comparison, the (R1) to (R3) branching ratio at 298 K calculated based on the rate coefficient for O_2+NO formation (R1)[30] and that for isotope exchange (R3)[28,29] is 60% to 40%. The difference between our best fit branching ratio of 52 to 48 and the rate coefficient ratio of 60 to 40 could arise from an energy dependence for the relative product yields since the average collision energy at 298 K is 0.6 kcal/mol, which is 5 to 15 times smaller than the experimental collision energy here, and a larger (R1) to (R3) branching ratio at lower collision energies is consistent with the negative temperature dependence of the $O(^3P)+NO_2 \rightarrow O_2+NO$ reaction (R1).[30] Alternatively, the branching ratios from these two methods may be equivalent within the combined experimental error, given the uncertainty ranges above, which include uncertainties in the angular distribution for O_2+NO formation (R1), and we note that the rate coefficient for isotope exchange (R3) has not been measured again since it was first measured in the 1960s. In any case, it is clear that isotope exchange is an important reaction channel for $^{18}O(^3P)+NO_2$.

For $^{18}O(^1D)+NO_2$, two product channels were observed: O_2+NO formation (R4) and quenching with isotope exchange (R5a), while two other possible product channels, $O(^1D)+NO_2$ quenching without isotope exchange (R5b) and isotope exchange without quenching (R6) were not observable above background (as noted in Table I). As is evident by inspection, O_2+NO formation is the major product channel for $O(^1D)+NO_2$. Our best estimate of the branching ratio for reaction to form O_2+NO versus quenching with isotope exchange (i.e., (R4) to (R5a)) is 97(+2/−12)% to 3(−12/+2)% from a comparison of the magnitudes of the high resolution $^{34}O_2$ signal corrected for $^{18}O(^3P)+NO_2$ in Figure 7 with the fast shoulder of the $^{48}NO_2$ signal in Figure 1. The primary uncertainty in this estimate stems from the uncertainty in the backward-peaking region of the angular distribution for $^{18}O(^1D)+NO_2$ isotope exchange, which was not sampled in the experiment (see Sec. III A); if we assume for the sake of argument that (R5a) is strongly backward peaking, we derive a conservative lower bound for the (R4) to (R5a) branching ratio of 85 to 15%. Conversely, if we use the most forward-peaking angular distribution for O_2+NO formation that is consistent with our data (see Figure 10) and a lower bound for the $O(^1D)+NO_2$ contribution to the isotope exchange signal of 10% (see Figure 1), we derive an upper bound for the (R4) to (R5a) branching ratio of 99 to 1%. Finally, we can estimate an upper bound for a possible contribution of quenching without isotope exchange (R5b) to the (R4) to ((R5a) + (R5b)) branching ratio by using the level of background in the $^{46}NO_2$ spectra at TOFs that would correspond to (R5b); we conclude that (R5b) can contribute at most ∼8% of the total $^{18}O(^1D)+NO_2$ reaction products. Clearly, in each case our conclusion that O_2+NO formation is the major product channel of $O(^1D)+NO_2$ is robust, confirming the hypothesis of Heidner and Husain,[15] who suggested that O_2+NO was the most likely product channel based on the large reaction exothermicity (∼92 kcal/mol). The estimate of 97(+2/−12)% to 3(−12/+2)% presented here for reaction versus isotope exchange ((R4) to (R5a)) for $O(^1D)+NO_2$ is the first to be derived from experiment.

D. Implications for atmospheric chemistry

While the primary conclusions of this work are new information on the dynamics, the nature of the intermediates, and the product branching ratios for the $O(^3P)+NO_2$ and $O(^1D)+NO_2$ reactions, implications of these results for atmospheric chemistry are briefly explored here. In particular, the crossed beam results showed that isotope exchange is a significant channel of the $O(^3P)+NO_2$ reaction, comparable in magnitude to the O_2+NO formation channel (with a branching ratio for O_2+NO formation versus isotope exchange derived from experiment of 52 to 48%). Furthermore, isotope exchange is a minor but non-negligible product channel of the $O(^1D)+NO_2$ reaction, representing 3% of the total product yield. Both these isotope exchange reactions have the potential to affect the isotopic composition of atmospheric NO_2, which in turn may affect the isotopic composition of nitrates, which has recently been used to distinguish between atmospheric deposition and biological production as sources of nitrate in various ecosystems.[31,32] The latter tracer studies depend on photochemical modeling of the oxygen isotopic compositions of NO_2 and HNO_3, and the $O(^3P)+NO_2$ and $O(^1D)+NO_2$ isotope exchange reactions investigated here are not included in these models.

More specifically, these tracer studies are based on the fact that NO_2 in the troposphere and stratosphere exhibit an "anomalous" ^{17}O isotopic signature,[33,34] in which the relationship between ^{17}O and ^{18}O deviates from that in oxygen-containing species in the terrestrial biosphere and oceans.[35] This anomalous signature originates in the ozone formation reaction,[36,37] which can then be transferred to NO_2 in the atmosphere via reactions including $O_3+NO \rightarrow NO_2+O_2$. These isotope anomalies do not originate outside of these atmospheric reactions and, hence, the magnitude of the ^{17}O anomaly in nitrates is used to partition between atmospheric (isotopically anomalous) and biological (isotopically normal) processes. A quantitative understanding of the reactions that control the magnitude of the anomalous isotopic signature of atmospheric NO_2 is required, and this in turn may depend on whether previously unconsidered mechanisms, such as the $O(^1D)+NO_2$ or $O(^3P)+NO_2$ isotope exchange reactions, can

affect the magnitude of the ^{17}O isotope anomaly in NO_2. In principle, the $O(^1D)+NO_2$ isotope exchange reaction could serve to increase the ^{17}O isotope anomaly in NO_2 since $O(^1D)$ originates from the photolysis of O_3 and thus carries the large anomaly of O_3. In contrast, the $O(^3P)+NO_2$ isotope exchange reaction might serve to decrease the ^{17}O isotope anomaly in NO_2 since $O(^3P)$ carries roughly the isotopic composition of atmospheric O_2 due to rapid isotope exchange between $O(^3P)$ and O_2.[33,38]

To test the sensitivity of the oxygen isotopic composition of NO_2 to the $O(^1D)+NO_2$ or $O(^3P)+NO_2$ isotope exchange reactions, output from a two-dimensional (latitude-altitude) atmospheric model[39] was input into several photochemical kinetics box (i.e., "0D") models that included isotopes. Results demonstrated that the $O(^1D)+NO_2$ isotope exchange reaction is never fast enough to alter the isotopic composition of NO_2 in either the troposphere or stratosphere (even if the branching yield for this reaction were as high as 15%) since the primary reaction by which the ^{17}O isotope anomaly is transferred from O_3 to NO_2 – the $O_3+NO\rightarrow NO_2+O_2$ reaction – is always orders of magnitude faster. Upon inclusion of the $O(^3P)+NO_2$ isotope exchange reaction, the magnitude of the ^{17}O anomaly of NO_2 remained unchanged for conditions at the surface but was reduced by ∼40 per mil at an altitude of 40 km where the rates of $O(^3P)+NO_2$ isotope exchange and $O_3+NO\rightarrow NO_2+O_2$ become comparable. Although the effects of atmospheric transport and the processing of NO_2 into HNO_3 were not included in this box model sensitivity study, we conclude that $O(^3P)+NO_2$ isotope exchange may alter the ^{17}O isotope anomaly in NO_2 in the stratosphere but not in the troposphere and will thus not likely affect measurements at Earth's surface.

IV. SUMMARY AND CONCLUSIONS

The reaction dynamics, reactive intermediates, and products formed upon collisions of $O(^3P)$ and $O(^1D)$ with NO_2 were examined using crossed atomic and molecular beams at 6.2 ± 3.2 and at 9.5 ± 0.6 kcal/mol. For both $^{18}O(^3P)+NO_2$ and $^{18}O(^1D)+NO_2$, reaction products corresponding to isotope exchange and O_2+NO formation were detected. Isotope exchange in the $^{18}O(^1D)+NO_2$ reaction was observed to occur in conjunction with quenching (R5a). The branching ratio for O_2+NO formation versus isotope exchange for $O(^3P)+NO_2$ was 52(+6/−2)% to 48(+2/−6)%, while that for $O(^1D)+NO_2$ was 97(+2/−12)% to 3(+12/−2)%, based on the measured product signal intensities and their uncertainties. For $O(^3P)+NO_2$, these results are consistent with the branching ratio for the $O(^3P)+NO_2$ reaction based on individual measurements of the rate coefficients for isotope exchange[28,29] vs. O_2+NO formation.[30] For $O(^1D)+NO_2$, these results represent the first direct determination of the branching ratio for O_2+NO formation vs. isotope exchange.

In addition to the branching ratios, product energy and angular distributions for $O(^3P)+NO_2$ isotope exchange (R3) and $O(^1D)+NO_2\rightarrow O_2+NO$ (R4) were derived. The $O(^3P)+NO_2$ isotope exchange reaction (R3) is characterized by a forward-backward symmetric angular distribution, indicating that it proceeds by an NO_3* complex that is long-lived with respect to its rotational period and that statistical incorporation of the reactant ^{18}O into the product NO_2 (apart from zero point energy isotope effects) likely occurs. In contrast, the $O(^1D)+NO_2\rightarrow O_2+NO$ reaction (R4) is characterized by a strongly forward-peaking angular distribution, signifying that it proceeds by a direct "stripping" mechanism via a short-lived ^{18}O-O-NO* complex, which is also consistent with our result that the reactant ^{18}O occurs exclusively in the O_2 product and not in the NO product. Furthermore, the product energy distribution derived for this reaction shows that the O_2+NO reaction products are formed with large amounts of internal energy (∼60 kcal/mol) and indicates the possible formation of electronically-excited product O_2 since both $O_2(a^1\Delta_g)$ and $O_2(b^1\Sigma_g^+)$ are energetically accessible. For $O(^3P)+NO_2\rightarrow O_2+NO$ (R1), the product energy and angular distributions are uncertain due to large amounts of background ^{34}S from the SO_2 photolysis source and to small signal in the high resolution O_2 photolysis experiments. However, we found that the reactant ^{18}O was detected only in the O_2 product and not the NO product, supporting the hypothesis that $O(^3P)+NO_2\rightarrow O_2+NO$ proceeds by an ^{18}O-O-NO* intermediate similar to that for $O(^1D)+NO_2\rightarrow O_2+NO$. Taken as a whole, our crossed beam results provide evidence for the formation of two distinct types of complexes upon the collision of oxygen atoms with NO_2: a long lived symmetric NO_3* complex that facilitates isotope exchange for $O(^3P)+NO_2$ (R3) and possibly for $O(^1D)+NO_2$ (R5), and an asymmetric peroxo-nitrate intermediate, OONO*, that results in the formation of O_2 and NO products ((R1) and (R4)).

ACKNOWLEDGMENTS

This material is based upon work supported in part by the U.S. National Science Foundation (NSF) under Grant No. CHE-0809973 to UC Berkeley and for NSF Graduate Research Fellowships for K.M. and for A.V. while at UC Berkeley. We also gratefully acknowledge support from the Berkeley Atmospheric Science Center for fellowships for K.M. and A.V., from The Camille Dreyfus Teacher-Scholar Award to K.B., from San Jose State University for start-up release time for A.V., and to The Institute of Atomic and Molecular Sciences from Academia Sinica. We thank Yu-Ju Lu for experimental assistance and Dr. Peter Connell for helpful atmospheric modeling discussions.

[1]H. F. Davis, B. S. Kim, H. S. Johnston, and Y. T. Lee, J. Phys. Chem. **97**(10), 2172 (1993).
[2]H. S. Johnston, H. F. Davis, and Y. T. Lee, J. Phys. Chem. **100**(12), 4713 (1996).
[3]K. Mikhaylichenko, C. Riehn, L. Valachovic, A. Sanov, and C. Wittig, J. Chem. Phys. **105**(16), 6807 (1996).
[4]W. Eisfeld and K. Morokuma, J. Chem. Phys. **114**(21), 9430 (2001).
[5]M. P. Grubb, M. L. Warter, K. M. Johnson, and S. W. North, J. Phys. Chem. A **115**(15), 3218 (2011).
[6]I. W. M. Smith, R. P. Tuckett, and C. J. Whitham, Chem. Phys. Lett. **200**(6), 615 (1992).
[7]M. A. A. Clyne and B. A. Thrush, Trans. Faraday Soc. **58**(471), 511 (1962).
[8]M. A. A. Clyne and B. A. Thrush, J. Chem. Phys. **38**(5), 1252 (1963).
[9]S. W. Benson, J. Chem. Phys. **38**(5), 1251 (1963).
[10]J. T. Herron and F. S. Klein, J. Chem. Phys. **40**(9), 2731 (1964).
[11]J. Troe, Ber. Bunsenges. Phys. Chem. **73**(8-9), 906 (1969).
[12]J. Troe and H. G. Wagner, Ann. Rev. Phys. Chem. **23**, 311 (1972).

[13]K. F. Preston and R. J. Cvetanovic, J. Chem. Phys. **45**(8), 2888 (1966).
[14]G. Paraskevopoulos, K. F. Preston, and R. J. Cvetanovic, J. Chem. Phys. **54**(9), 3907 (1971).
[15]R. F. Heidner and D. Husain, Int. J. Chem. Kinet. **5**(5), 819 (1973).
[16]M. J. E. Gauthier and D. R. Snelling, J. Photochem. **4**(1–2), 27 (1975).
[17]M. J. Perri, A. L. Van Wyngarden, K. A. Boering, J. J. Lin, and Y. T. Lee, J. Chem. Phys. **119**(16), 8213 (2003).
[18]M. J. Perri, A. L. Van Wyngarden, J. J. Lin, Y. T. Lee, and K. A. Boering, J. Phys. Chem. A **108**(39), 7995 (2004).
[19]R. D. Levine and R. B. Bernstein, *Molecular Reaction Dynamics and Chemical Reactivity* (Oxford University Press, New York, 1987).
[20]J. J. Lin, D. W. Hwang, S. Harich, Y. T. Lee, and X. M. Yang, Rev. Sci. Instrum. **69**(4), 1642 (1998).
[21]U. Even, J. Jortner, D. Noy, N. Lavie, and C. Cossart-Magos, J. Chem. Phys. **112**(18), 8068 (2000).
[22]W. F. Giauque and J. D. Kemp, J. Chem. Phys. **6**(1), 40 (1938).
[23]J. J. Lin, S. Harich, Y. T. Lee, and X. Yang, J. Chem. Phys. **110**(22), 10821 (1999).
[24]M. Brouard, R. Cireasa, A. P. Clark, T. J. Preston, C. Vallance, G. C. Groenenboorn, and O. S. Vasyutinskii, J. Phys. Chem. A **108**(39), 7965 (2004).
[25]See supplementary material at http://dx.doi.org/10.1063/1.4736567 for supplementary figures.
[26]See http://physics.nist.gov/PhysRefData/Ionization/ for electron impact ionization cross sections.
[27]See http://webbook.nist.gov for mass fragmentation patterns.
[28]F. S. Klein and J. T. Herron, J. Chem. Phys. **41**(5), 1285 (1964).
[29]F. S. Klein and J. T. Herron, J. Chem. Phys. **44**, 3645 (1966).
[30]S. P. Sander, J. Abbatt, J. R. Barker, J. B. Burkholder, R. R. Friedl, D. M. Golden, R. E. Huie, C. E. Kolb, M. J. Kurylo, G. K. Moortgat, V. L. Orkin, and P. H. Wine, "Chemical Kinetics and Photochemical Data for Use in Atmospheric Studies," Evaluation No. 17, JPL Publication 10-6, NASA Jet Propulsion Laboratory, Pasadena, CA, 2011.
[31]G. Michalski, J. K. Bohlke, and M. Thiemens, Geochim. Cosmochim. Acta **68**(20), 4023 (2004).
[32]G. Michalski, J. G. Bockheim, C. Kendall, and M. Thiemens, Geophys. Res. Lett. **32**(13), 13817, doi:10.1029/2004GL022121 (2005).
[33]J. R. Lyons, Geophys. Res. Lett. **28**(17), 3231, doi:10.1029/2000GL012791 (2001).
[34]G. Michalski, Z. Scott, M. Kabiling, and M. H. Thiemens, Geophys. Res. Lett. **30**(16), 1870, doi:10.1029/2003GL017015 (2003).
[35]Y. Matsuhisa, J. R. Goldsmith, and R. N. Clayton, Geochim. Cosmochim. Acta **42**(2), 173 (1978).
[36]J. Morton, J. Barnes, B. Schueler, and K. Mauersberger, J. Geophys. Res.-Atmos. **95**(D1), 901 (1990).
[37]K. Mauersberger, B. Erbacher, D. Krankowsky, J. Gunther, and R. Nickel, Science **283**(5400), 370 (1999).
[38]M. R. Wiegell, N. W. Larsen, T. Pedersen, and H. Egsgaard, Int. J. Chem. Kinet. **29**(10), 745 (1997).
[39]K. A. Mar, M. C. McCarthy, P. Connell, and K. A. Boering, J. Geophys. Res.-Atmos. **112**(D19), D19302 (2007).